Progress In Electromagnetics Research, PIER 42, 193–218, 2003

ASYMPTOTIC RADIATION FIELD OF ASYMMETRIC PLANAR DIELECTRIC WAVEGUIDE

J.-S. Lee

University of Illinois at Urbana-Champaign
Department of Electrical and Computer Engineering
464 Everitt Laboratory
1406 W. Green Str., Urbana, IL 61801, USA

D. P. Nyquist

Michigan State University
Department of Electrical and Computer Engineering
C132 Engineering Research Complex, MI, USA

Abstract—This paper describes the steepest-descent evaluation of the radiation field for both TE and TM modes of an asymmetric planar open waveguide. The cover, film and substrate field will be formulated in the spectral domain. The steepest-descent path in the complex axial transform plane (ζ-plane) is identified as a direct method and that in the complex ϕ-plane ($\phi = \sigma + j\eta$: complex polar coordinate) is also identified as an indirect method in order to validate the steepest-descent path in the complex axial transform plane (ζ-plane). The branch cut integration will be rigorously analyzed through complex-phasor diagrams. An alternative integration path will be also identified since it is an effective method to validate the steepest-descent and branch cut integrations. Then, the steepest-descent evaluation of cover and substrate fields and numerical results for TE modes will be presented and numerical implementation for TM modes will be accommodated in the future research.

1. INTRODUCTION AND GEOMETRICAL CONFIGURATION

The steepest-descent method in the complex ϕ-plane has been extensively developed to determine the asymptotic radiation field of planar waveguide structures [1–4]. Due to the intrinsic nature of complexity in the complex ϕ-plane, the radiation fields of open planar waveguides are identified and classified here through the steepest-descent method in the complex axial transform plane [5, 6]. The spectral fields of planar open waveguide structures possess multiple branch points associated with each of the three planar layers. The branch point associated with the film layer is removable and the branch points associated with the cover layer and the substrate layers are non-removable. The steepest-descent evaluation of radiation fields in both the cover and the substrate layer maintained by TE or TM electric sources in proximity to the simplest canonical waveguide structure will be performed when spectral representations of those fields possess multiple non-removable branch points in the complex axial transform plane.

For the TE or TM cover field, the steepest-descent path in the complex axial transform plane replaces the cover layer branch cut while the substrate layer branch cut is retained. Alternatively the cover and the incomplete substrate layer branch cut are replaced while the remaining substrate layer branch cut is retained. However, in the substrate layer, the incomplete cover and the complete substrate layer branch cut are replaced while the remaining cover layer branch cut is retained.

The numerical results are only presented for TE case and numerical implementation for TM case will be accommodated in future research.

The planar waveguide structure consists of a dielectric guiding region immersed in a planar-layered background environment. Each

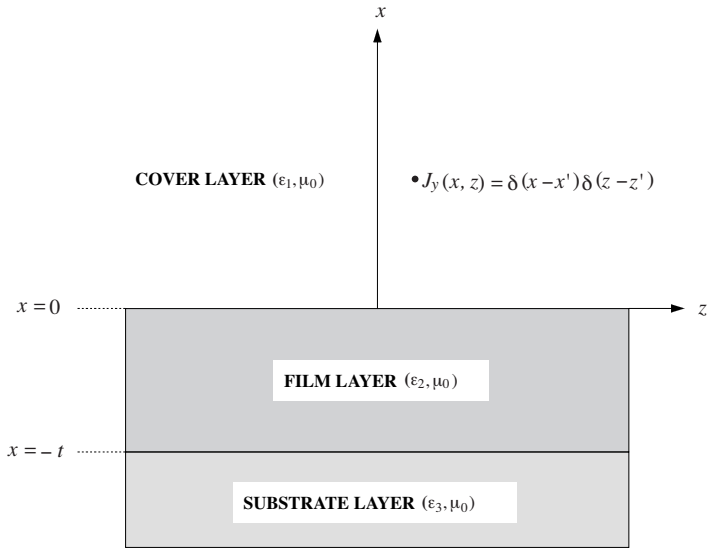

Figure 1. Geometrical configuration of an asymmetric planar dielectric slab waveguide with TE line-source excitation. Cover, film, and substrate layers are considered in the low-loss limit.

planar layer is non-magnetic, isotropic, and homogeneous with complex permittivity ε_l, $l = 1, 2, 3$ for cover, film, and substrate layers. A coordinate system is chosen with the z axis as the waveguiding axis and the x axis normal to the planar interfaces as depicted in Figures 1 and 2 for TE and TM modes respectively. The structure is of infinite extent parallel to the y-z plane.

2. SPECTRAL TE FIELD FORMULATION

Uniformity along the waveguiding axis z prompts a complex axial Fourier transformation of all field quantities with respect to the z variable. Since the spectral fields are TE with respect to the waveguiding axis in agreement with the prescribed y-invariance, the guided wave fields are

$$\begin{aligned} \tilde{\boldsymbol{e}}(\boldsymbol{x}, \boldsymbol{\zeta}) &= \hat{y}\tilde{e}_y(x, \zeta) \\ \tilde{\boldsymbol{h}}(\boldsymbol{x}, \boldsymbol{\zeta}) &= \hat{x}h_x(x, \zeta) + \hat{z}h_z(x, \zeta) \end{aligned} \tag{1}$$

where $\tilde{\boldsymbol{e}}(\boldsymbol{x}, \boldsymbol{\zeta})$ and $\tilde{\boldsymbol{h}}(\boldsymbol{x}, \boldsymbol{\zeta})$ are ζ-transform pairs of $\boldsymbol{E}(\boldsymbol{x}, \boldsymbol{z})$ and $\boldsymbol{H}(\boldsymbol{x}, \boldsymbol{z})$ respectively. Unit line current source excitation ($e^{j\omega t}$ time dependence)

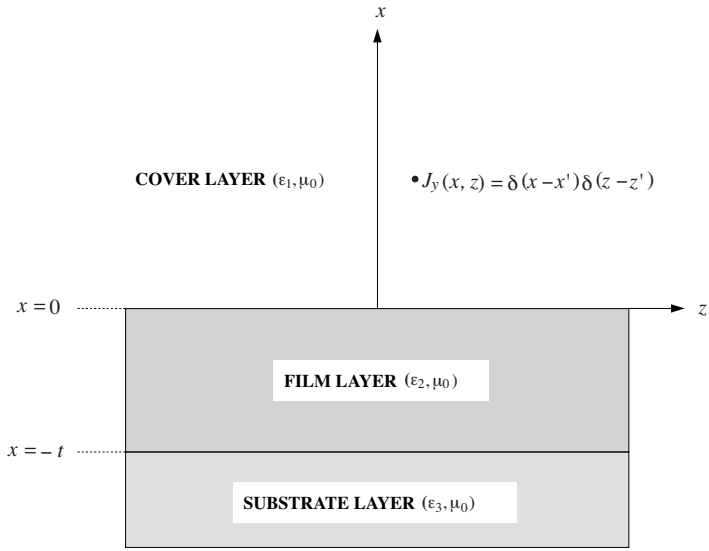

Figure 2. Geometrical configuration of an asymmetric planar dielectric slab waveguide with TM line-source excitation. Cover, film, and substrate layers are considered in the low-loss limit.

is assumed. The spectral Maxwellian equations for the l'th layer become

$$\begin{aligned} \zeta\tilde{e}_y(x,\zeta) &= \omega\mu_0\tilde{h}_x(x,\zeta) \\ \frac{\partial\tilde{e}_y(x,\zeta)}{\partial x} &= -j\omega\mu_0\tilde{h}_z(x,\zeta) \\ j\zeta\tilde{h}_x(x,\zeta) - \frac{\partial\tilde{h}_z(x,\zeta)}{\partial x} &= \tilde{j}_y(x,\zeta) + j\omega\varepsilon_l\tilde{e}_y(x,\zeta) \end{aligned} \tag{2}$$

where $\tilde{j}_y(x,\zeta) = \delta(x-x')e^{-j\zeta z'}$. Subsequent manipulation uncouples the spectral Maxwell equations to yield the spectral Helmholtz equation.

$$\frac{\partial^2\tilde{e}_y(x,\zeta)}{\partial x^2} - p_l^2(\zeta)\tilde{e}_y(x,\zeta) = j\omega\mu_0\tilde{j}_y(x,\zeta) \tag{3}$$

where $p_l(\zeta) = \sqrt{\zeta^2 - k_l^2}$ $(l = 1,2,3)$ and $k_l = n_l k_0$ $(n_l = \sqrt{\varepsilon_l/\varepsilon_0})$. The spectral cover field decomposes into the principal and reflected field and Eqn. (4) superposes the primary and reflected solution in

agreement with Eqn. (3).

$$\begin{aligned}\tilde{e}^{p}_{1y}(x,\zeta) &= -j\omega\mu_0 \frac{e^{-p_1(\zeta)|x-x'|}}{2p_1(\zeta)} e^{-j\zeta z'} \\ \tilde{e}^{r}_{1y}(x,\zeta) &= -j\omega\mu_0 R(\zeta) \frac{e^{-p_1(\zeta)(x+x')}}{2p_1(\zeta)} e^{-j\zeta z'}\end{aligned} \tag{4}$$

where $R(\zeta)$ denotes the reflection coefficient given by

$$R(\zeta) = \frac{(p_1 - p_3)p_2 + (p_1 p_3 - p_2^2)\tanh(p_2 t)}{(p_1 + p_3)p_2 + (p_1 p_3 + p_2^2)\tanh(p_2 t)} \tag{5}$$

The film field decomposes into the transmitted and reflected fields

$$\tilde{e}_{2y}(x,\zeta) = -j\omega\mu_0 C(\zeta)\left[e^{p_2(\zeta)x} + \overline{R}(\zeta)e^{-p_2(\zeta)(x+2t)}\right]\frac{e^{-p_1(\zeta)x'}}{2p_1(\zeta)} e^{-j\zeta z'} \tag{6}$$

where $C(\zeta)$ is the coupling and $\overline{R}(\zeta)$ is the interfacial reflection coefficient given by

$$\begin{aligned}C(\zeta) &= \frac{2p_1(p_2 + p_3)}{(1 + e^{-2p_2 t})\, Z(\zeta)} \\ \overline{R}(\zeta) &= \frac{p_2 - p_3}{p_2 + p_3}\end{aligned} \tag{7}$$

where $Z(\zeta) = (p_1 + p_3)p_2 + (p_1 p_3 + p_2^2)\tanh(p_2 t)$. The spectral substrate field is the transmitted field only and given by

$$\tilde{e}_{3y}(x,\zeta) = -j\omega\mu_0 T(\zeta) e^{p_3(\zeta)(x+t)} \frac{e^{-p_1(\zeta)x'}}{2p_1(\zeta)} e^{-j\zeta z'} \tag{8}$$

where $T(\zeta)$ is the transmission coefficient defined by

$$T(\zeta) = \frac{2p_1 p_2}{\cosh(p_2 t) Z(\zeta)} \tag{9}$$

where $Z(\zeta)$ is given earlier.

3. SPECTRAL TM FIELD FORMULATION

Since the spectral fields are TM with respect to the waveguiding axis z,

$$\begin{aligned}\tilde{\boldsymbol{e}}_{\boldsymbol{l}}(\boldsymbol{x},\boldsymbol{\zeta}) &= \hat{x}\tilde{e}_{lx}(x,\zeta) + \hat{z}\tilde{e}_{lz}(x,\zeta) \\ \tilde{\boldsymbol{h}}_{\boldsymbol{l}}(\boldsymbol{x},\boldsymbol{\zeta}) &= \hat{y}\tilde{h}_{ly}(x,\zeta)\end{aligned} \tag{10}$$

y-invariant current source excitation is assumed. The spectral Maxwellian equations for the l'th ($l = 1, 2, 3$ *for cover, film and substrate*) layer become

$$\begin{aligned}
&\left(\tilde{\nabla}_t + \hat{z}j\zeta\right) \cdot \tilde{\boldsymbol{e}}_{\boldsymbol{l}}(\boldsymbol{x}, \boldsymbol{\zeta}) = \hat{\rho}(x, \zeta)/\varepsilon_l \\
&\left(\tilde{\nabla}_t + \hat{z}j\zeta\right) \times \tilde{\boldsymbol{e}}_{\boldsymbol{l}}(\boldsymbol{x}, \boldsymbol{\zeta}) = -j\omega\mu_0 \tilde{\boldsymbol{h}}_{\boldsymbol{l}}(\boldsymbol{x}, \boldsymbol{\zeta}) \\
&\left(\tilde{\nabla}_t + \hat{z}j\zeta\right) \times \tilde{\boldsymbol{h}}_{\boldsymbol{l}}(\boldsymbol{x}, \boldsymbol{\zeta}) = \tilde{\boldsymbol{j}}(\boldsymbol{x}, \boldsymbol{\zeta}) + j\omega\varepsilon_l \tilde{\boldsymbol{e}}_{\boldsymbol{l}}(\boldsymbol{x}, \boldsymbol{\zeta}) \\
&\left(\tilde{\nabla}_t + \hat{z}j\zeta\right) \cdot \tilde{\boldsymbol{h}}_{\boldsymbol{l}}(\boldsymbol{x}, \boldsymbol{\zeta}) = 0
\end{aligned} \tag{11}$$

where $\tilde{\nabla}_t = \hat{x}\frac{\partial}{\partial x} + \hat{y}\frac{\partial}{\partial y}$ and $\tilde{\boldsymbol{j}}(\boldsymbol{x}, \boldsymbol{\zeta}) = \hat{x}\tilde{j}_x(x, \zeta) + \hat{z}\tilde{j}_z(x, \zeta)$.

The transverse/longitudinal decomposition of independent Maxwellian equations yields

$$\begin{aligned}
\tilde{\boldsymbol{e}}_{\boldsymbol{lt}}(\boldsymbol{x}, \boldsymbol{\zeta}) &= -\frac{1}{p_l^2}\left\{j\zeta\tilde{\nabla}_t\tilde{e}_{lz}(x, \zeta) + j\omega\mu_0\tilde{\boldsymbol{j}}_{\boldsymbol{x}}(\boldsymbol{x}, \boldsymbol{\zeta})\right\} \\
\tilde{\boldsymbol{h}}_{\boldsymbol{lt}}(\boldsymbol{x}, \boldsymbol{\zeta}) &= -\frac{1}{p_l^2}\left\{-j\omega\varepsilon_l\hat{z} \times \tilde{\nabla}_t\tilde{e}_{lz}(x, \zeta) - j\zeta\hat{z} \times \hat{x}\tilde{j}_x(x, \zeta)\right\}
\end{aligned} \tag{12}$$

Subsequent manipulation uncouples the spectral Maxwellian equations to obtain the spectral Helmholtz equations.

$$\begin{aligned}
\tilde{\nabla}_t^2\tilde{e}_{lz}(x, \zeta) - p_l^2(\zeta)\tilde{e}_{lz}(x, \zeta) &= \frac{j\zeta}{\varepsilon_l}\tilde{\rho}(x, \zeta) + j\omega\mu_0\tilde{j}_z(x, \zeta) \\
\tilde{\nabla}_t^2\tilde{h}_{lz}(x, \zeta) - p_l^2(\zeta)\tilde{h}_{lz}(x, \zeta) &= -\hat{z} \cdot \left\{\tilde{\nabla}_t \times \tilde{\boldsymbol{j}}_{\boldsymbol{t}}(\boldsymbol{x}, \boldsymbol{\zeta})\right\}
\end{aligned} \tag{13}$$

Spectral continuity equation $\nabla \cdot \tilde{\boldsymbol{j}}(\boldsymbol{x}, \boldsymbol{\zeta}) + j\omega\tilde{\rho}(x, \zeta) = 0$ allows Eqn. (13) to be

$$\begin{aligned}
\tilde{\nabla}_t^2\tilde{e}_{lz}(x, \zeta) - p_l^2(\zeta)\tilde{e}_{lz}(x, \zeta) &= -\frac{\zeta}{\omega\varepsilon_l}\left(\tilde{\nabla}_t + \hat{z}j\zeta\right) \cdot \tilde{\boldsymbol{j}}(\boldsymbol{x}, \boldsymbol{\zeta}) + j\omega\mu_0\tilde{j}_z(x, \zeta) \\
\tilde{\nabla}_t^2\tilde{h}_{lz}(x, \zeta) - p_l^2(\zeta)\tilde{h}_{lz}(x, \zeta) &= -\hat{z} \cdot \left\{\tilde{\nabla}_t \times \tilde{\boldsymbol{j}}_{\boldsymbol{t}}(\boldsymbol{x}, \boldsymbol{\zeta})\right\}
\end{aligned} \tag{14}$$

It is observed that $\tilde{e}_{lz}(x, \zeta)$ is the spectral-field generating function and given by

$$\left[\frac{\partial^2}{\partial x^2} - p_l^2(\zeta)\right]\tilde{e}_{lz}(x, \zeta) = -\frac{\zeta}{\omega\varepsilon_l}\frac{\partial\tilde{j}_x(x, \zeta)}{\partial x} - \frac{jp_l^2(\zeta)}{\omega\varepsilon_l}\tilde{j}_z(x, \zeta) \tag{15}$$

Even if the spectral field formulation can be done by the well-known electric vector potential approach, the proposed methodology

can be easily applied to extract the spectral Green's dyads [7–9] which completely determine the spectral EM fields for the l'th layer ($l = 1, 2, 3$). Both electric and magnetic spectral fields are represented by spectral Green's dyads where $\overline{\boldsymbol{g}}^{\boldsymbol{e}}_{\boldsymbol{lm}}(\boldsymbol{x}|\boldsymbol{x}')$ and $\overline{\boldsymbol{g}}^{\boldsymbol{h}}_{\boldsymbol{lm}}(\boldsymbol{x}|\boldsymbol{x}')$ represent the spectral Green's dyads for the spectral electric and magnetic fields respectively in the l'th layer due to currents in or interactions with the m'th layer (see Appendix A).

$$
\begin{aligned}
\tilde{\boldsymbol{e}}_{\boldsymbol{1}}(\boldsymbol{x},\boldsymbol{\zeta}) &= \int_0^\infty \left[\overline{\boldsymbol{g}}^{\boldsymbol{e}}_{\boldsymbol{11}}(\boldsymbol{x}|\boldsymbol{x}') + \overline{\boldsymbol{g}}^{\boldsymbol{e}}_{\boldsymbol{12}}(\boldsymbol{x}|\boldsymbol{x}')\right] \cdot \tilde{\boldsymbol{j}}(\boldsymbol{x}',\boldsymbol{\zeta})dx' \\
\tilde{\boldsymbol{e}}_{\boldsymbol{2}}(\boldsymbol{x},\boldsymbol{\zeta}) &= \int_0^\infty \overline{\boldsymbol{g}}^{\boldsymbol{e}}_{\boldsymbol{21}}(\boldsymbol{x}|\boldsymbol{x}') \cdot \tilde{\boldsymbol{j}}(\boldsymbol{x}',\boldsymbol{\zeta})dx' \\
\tilde{\boldsymbol{e}}_{\boldsymbol{3}}(\boldsymbol{x},\boldsymbol{\zeta}) &= \int_0^\infty \overline{\boldsymbol{g}}^{\boldsymbol{e}}_{\boldsymbol{31}}(\boldsymbol{x}|\boldsymbol{x}') \cdot \tilde{\boldsymbol{j}}(\boldsymbol{x}',\boldsymbol{\zeta})dx' \\
\tilde{\boldsymbol{h}}_{\boldsymbol{1}}(\boldsymbol{x},\boldsymbol{\zeta}) &= \int_0^\infty \left[\overline{\boldsymbol{g}}^{\boldsymbol{h}}_{\boldsymbol{11}}(\boldsymbol{x}|\boldsymbol{x}') + \overline{\boldsymbol{g}}^{\boldsymbol{h}}_{\boldsymbol{12}}(\boldsymbol{x}|\boldsymbol{x}')\right] \cdot \tilde{\boldsymbol{j}}(\boldsymbol{x}',\boldsymbol{\zeta})dx' \\
\tilde{\boldsymbol{h}}_{\boldsymbol{2}}(\boldsymbol{x},\boldsymbol{\zeta}) &= \int_0^\infty \overline{\boldsymbol{g}}^{\boldsymbol{h}}_{\boldsymbol{21}}(\boldsymbol{x}|\boldsymbol{x}') \cdot \tilde{\boldsymbol{j}}(\boldsymbol{x}',\boldsymbol{\zeta})dx' \\
\tilde{\boldsymbol{h}}_{\boldsymbol{3}}(\boldsymbol{x},\boldsymbol{\zeta}) &= \int_0^\infty \overline{\boldsymbol{g}}^{\boldsymbol{h}}_{\boldsymbol{31}}(\boldsymbol{x}|\boldsymbol{x}') \cdot \tilde{\boldsymbol{j}}(\boldsymbol{x}',\boldsymbol{\zeta})dx'
\end{aligned}
\tag{16}
$$

It is noted in Appendix A that

$$
\tilde{\Lambda} = \frac{2p_1p_2}{(\varepsilon_2p_3 - \varepsilon_3p_2)(\varepsilon_1p_2 - \varepsilon_2p_1)e^{-p_2t} + (\varepsilon_2p_3 + \varepsilon_3p_2)(\varepsilon_1p_2 + \varepsilon_2p_1)e^{p_2t}} \tag{17}
$$

Each scalar component of the spectral EM fields is completely determined by the spectral Green's dyad above and the spectral current density $\tilde{\boldsymbol{j}}(\boldsymbol{x},\boldsymbol{\zeta}) = \hat{x}\tilde{j}_x(x,\zeta) + \hat{z}\tilde{j}_z(x,\zeta)$.

4. STEEPEST-DESCENT PATH IN THE COMPLEX AXIAL TRANSFORM PLANE (ζ-PLANE)

Transformation to spatial polar coordinates (r, θ) in both transverse and longitudinal representations is implemented as depicted in Fig. 3.

As depicted in Fig. 4, for the phase-corrected TE cover field,

$$
\begin{aligned}
|x - x'| &= r\cos\theta - x'\cos^2\theta \\
x + x' &= r\cos\theta + x'\cos^2\theta \\
z - z' &= r\sin\theta
\end{aligned}
\tag{18}
$$

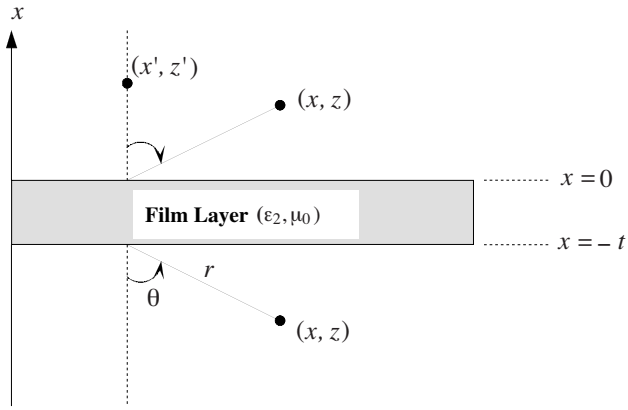

Figure 3. Polar coordinate transformations for TE modes.

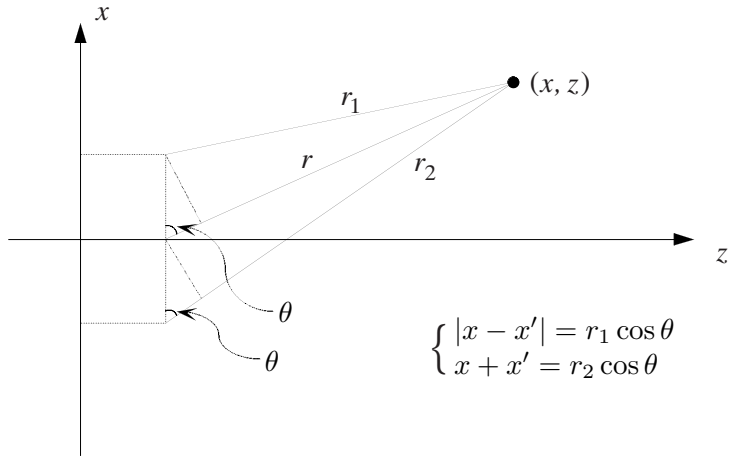

Figure 4. Phase correction diagram in the cover layer.

For the TE substrate field,

$$\begin{aligned} x + t &= -r\cos\theta \\ z - z' &= r\sin\theta \end{aligned} \tag{19}$$

Substituting Eqn. (18) into Eqn. (4) and subsequent inverse Fourier transformation yield the spatial cover field as

$$E_{1y}(x,z) = C_0 \int_{-\infty}^{\infty} \frac{1 + R'(\zeta)}{p_1(\zeta)} e^{p_1(\zeta)x'\cos^2\theta} e^{r[-j\zeta\sin\theta - p_1(\zeta)\cos\theta]} d\zeta \tag{20}$$

where $R'(\zeta) = R(\zeta)e^{-2p_1(\zeta)x'\cos^2\theta}$ and $C_0 = -j\omega\mu_0/4\pi$. The spatial substrate field is, in agreement with Eqns. (8) and (18), recovered as

$$E_{3y}(x,z) = -j\omega\mu_0 \int_{-\infty}^{\infty} T(\zeta)\frac{e^{-p_1(\zeta)x'}}{4\pi p_1(\zeta)} e^{r[-j\zeta\sin\theta - p_3(\zeta)\cos\theta]}d\zeta \tag{21}$$

Eqns. (20) and (21) lead to identification of $\delta(\zeta)$ such that

$$\delta(\zeta) = -j\zeta\sin\theta - p_l(\zeta)\cos\theta \tag{22}$$

where $l = 1$ and 3 for cover and substrate layers respectively. The stationary point ζ_0 in the complex ζ-plane was shown to be the *saddle point* in that plane [10]. Then,

$$\delta'(\zeta_0) = 0 \tag{23}$$

where $\zeta_0 = k_l \sin\theta$ and the observation aspect angle is defined by

$$\theta = \begin{cases} l = 1 : \begin{cases} \tan^{-1}\{(z-z')/|x-x'|\} \\ \tan^{-1}\{(z-z')/(x+x')\} \end{cases} \\ l = 3 : \tan^{-1}\{(z-z')/|x+t|\} \end{cases} \tag{24}$$

Hence, the steepest-descent path in the complex ζ-plane is identified as

$$\delta(\zeta) = \delta(\zeta_0) \tag{25}$$

After some manipulation,

$$\left(\frac{\zeta}{k_l}\right)\sin\theta - j\left[\frac{p_l(\zeta)}{k_l}\right]\cos\theta = 1 \tag{26}$$

Consequently, the steepest-descent path in the complex ζ-plane is obtained by

$$\left[\frac{\zeta}{k_l} + \left(\frac{\zeta}{k_l}\right)^*\right]\frac{\sin\theta}{2} - j\left[\frac{p_l(\zeta)}{k_l} - \left\{\frac{p_l(\zeta)}{k_l}\right\}^*\right]\frac{\cos\theta}{2} = 1 \tag{27}$$

where asterisk * indicates the complex conjugate. Eqn. (27) is confirmed by the well-known steepest-descent path in the complex polar coordinate $\phi = \sigma + j\eta$.

For TM modes, the steepest-descent path for the Green's dyad representation rather than for the field representation is chosen to be considered. The spatial Green's dyads are

$$\begin{aligned} \tilde{\boldsymbol{G}}_{\boldsymbol{l}}^{\boldsymbol{e}}(\boldsymbol{x},\boldsymbol{z}|\boldsymbol{x}',\boldsymbol{z}') &= \frac{1}{2\pi}\int_{-\infty}^{\infty} \overline{\boldsymbol{g}}_{\boldsymbol{l}}^{\boldsymbol{e}}(\boldsymbol{x}|\boldsymbol{x}')e^{j\zeta(z-z')}d\zeta \\ \tilde{\boldsymbol{G}}_{\boldsymbol{l}}^{\boldsymbol{h}}(\boldsymbol{x},\boldsymbol{z}|\boldsymbol{x}',\boldsymbol{z}') &= \frac{1}{2\pi}\int_{-\infty}^{\infty} \overline{\boldsymbol{g}}_{\boldsymbol{l}}^{\boldsymbol{h}}(\boldsymbol{x}|\boldsymbol{x}')e^{j\zeta(z-z')}d\zeta \end{aligned} \tag{28}$$

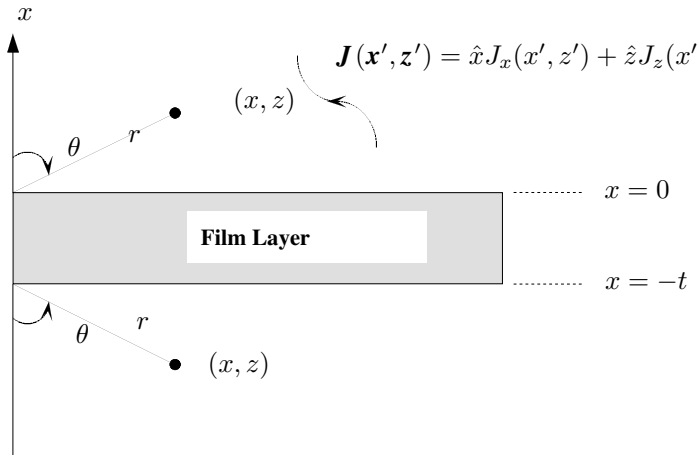

Figure 5. Polar coordinate transformations for TM modes.

For far zone,

$$x \gg x' \rightarrow |x - x'| = x - x' \tag{29}$$

As depicted in Fig. 5, for the cover field,

$$\begin{aligned} x &= r\cos\theta \\ z &= r\sin\theta \end{aligned} \tag{30}$$

For the substrate field,

$$\begin{aligned} x + t &= -r\cos\theta \\ z &= r\sin\theta \end{aligned} \tag{31}$$

Then, the subsequent manipulation leads to the identical $\delta(\zeta)$ as obtained in Eqn. (22), which is not repeated here. The steepest-descent path in the complex ζ-plane for TM modes is exactly determined by Eqn. (27), which is identical for TE modes.

5. BRANCH CUT

It is observed that

$$\left.\begin{array}{l} \mathrm{Re}\,\{p_l(\zeta)\} > 0 \cdots \text{for all } \zeta \\ \mathrm{Im}\,\{p_l(\zeta)\} > 0 \cdots \text{for real } \zeta \end{array}\right\} \cdots p_l(\zeta) = \sqrt{\zeta^2 - k_l^2},\ l = 1, 2, 3 \tag{32}$$

is necessary to satisfy the radiation condition. Hence, the branch cut is defined by

$$\mathrm{Re}\,\{p_l(\zeta)\} = 0 \tag{33}$$

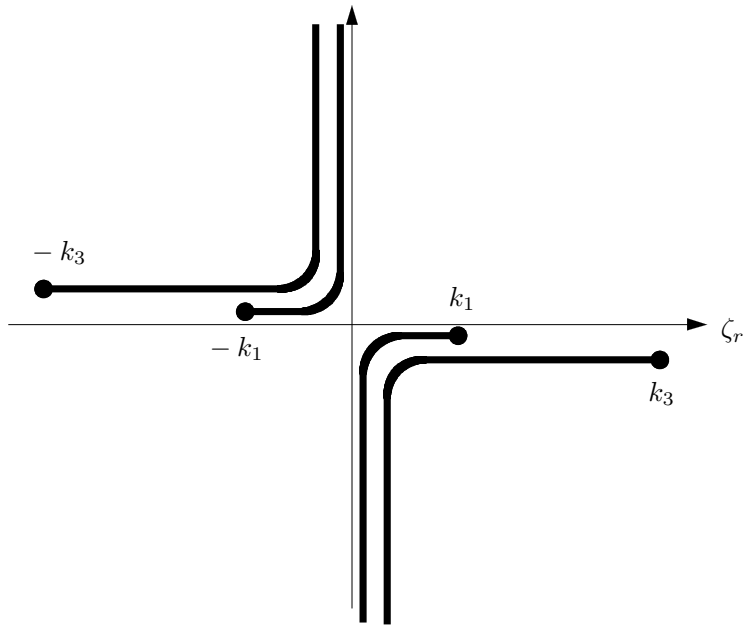

Figure 6. Branch cut construction in the low-loss limit.

Since the integrands of integral representations are not even in $p_1(\lambda)$ and $p_3(\zeta)$, the branch points contributed by the cover and the substrate layer are non-removable. Then,

$$\begin{aligned} &\zeta_r \zeta_i = k_{lr} k_{li} \\ &\zeta_r^2 - \zeta_i^2 < k_{lr}^2 - k_{li}^2 \end{aligned} \tag{34}$$

constructs *branch cuts* emanating from $\zeta_i = k_{li}$ at $\zeta_r = k_{lr}$ with $\zeta_i \to \infty$ as $\zeta_r \to 0$ in the low-loss limit as depicted in Fig. 6. Portions of the various cuts coalesce upon one another but they are a little exaggerated to be clarified.

It is required to analyze a complex-phasor diagram in the complex ζ-plane as depicted in Fig. 7 to implement the integration along the branch cut. The Re$\{\zeta\}$-axis inversion contour can be deformed to the infinite semicircle in the upper half plane or in the lower half plane with appropriate detour about the branch cuts as shown. Also appropriate choice of branch cuts consequently leads to a 4-sheeted Riemann surface in the complex ζ-plane. For a point 1 in Fig. 7,

$$p_1(\zeta) = \sqrt{\rho^+ \rho^-}\, e^{j(-\pi+\psi-\psi)/2} = -j|p_1(\zeta)| \tag{35}$$

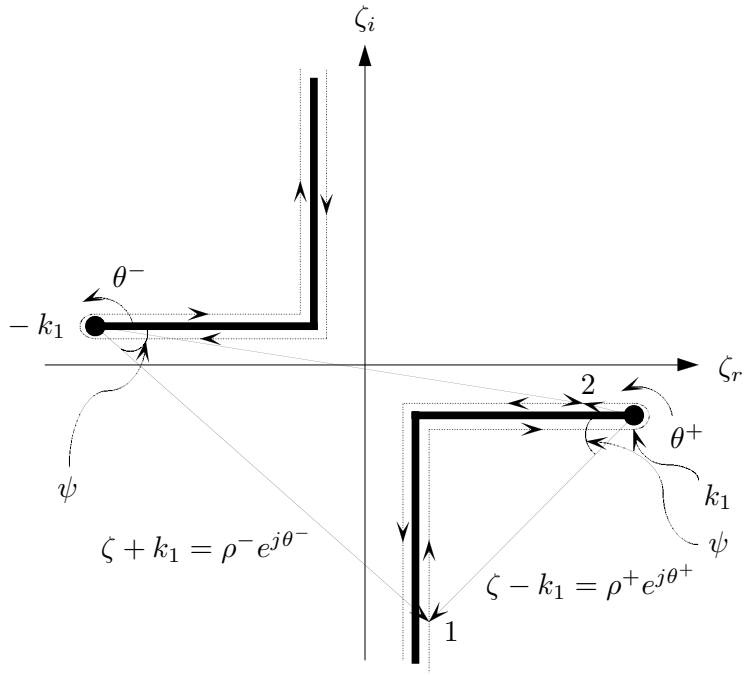

Figure 7. Complex-phasor diagram in the complex ζ-plane.

Similarly, for an opposite point on the left part of the negative imaginary branch cut,

$$p_1(\zeta) = \sqrt{\rho^+\rho^-}e^{j(\pi+\psi-\psi)/2} = j|p_1(\zeta)| \tag{36}$$

And also for a point 2 in Fig. 7,

$$p_1(\zeta) = \sqrt{\rho^+\rho^-}e^{j(\pi+0)/2} = j|p_1(\zeta)| \tag{37}$$

Similarly, for an opposite point on the lower part of the positive real branch cut,

$$p_1(\zeta) = \sqrt{\rho^+\rho^-}e^{j(-\pi+0)/2} = -j|p_1(\zeta)| \tag{38}$$

It is noted that the previous complex-phasor diagram analysis can be complied with that during the integration along the substrate layer branch cut and branch points $\pm k_3$.

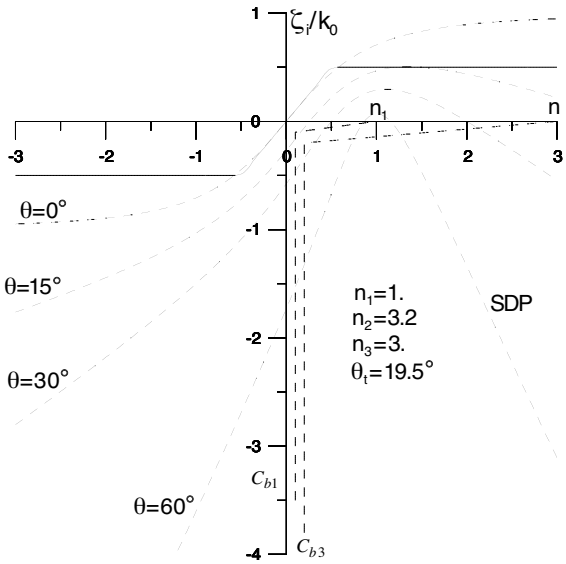

Figure 8. The steepest-descent paths for the cover layer field calculation on various observation aspect angles in the complex axial spectral plane. The asymmetric planar dielectric waveguide consists of cover, guiding and substrate layer with indices $n_1 = 1,\ n_2 = 3.2$, and $n_3 = 3$ respectively.

6. STEEPEST-DESCENT EVALUATION OF COVER FIELD

Mapping to the complex ϕ-plane deforms the path of integration, in which case the simple representation in terms of a discrete (bound) and continuous spectrum is severely compromised due to the complicated branch cut mapping. It is consequently more convenient to use the steepest-descent path in the complex ζ-plane since all the field quantities are represented on the same spectral domain. The steepest-descent path on the complex ζ-plane is explicitly derived from Eqn. (27) such that

$$\zeta'' = \pm \frac{|\zeta' - k_l \sin\theta||k_l - \zeta' \sin\theta|}{\cos\theta\sqrt{(\zeta'\cos\theta)^2 + (k_l - \zeta'\sin\theta)^2}} \tag{39}$$

where $\zeta = \zeta' + j\zeta'' = (\zeta', \zeta'')$. It is observed that one of ζ'-intercepts, $\zeta' = k_l \sin\theta$, matches the saddle point. Fig. 8 depicts the steepest-descent paths for the cover field in the complex ζ-plane for various observation aspect angles. As depicted in Fig. 8, the steepest-descent

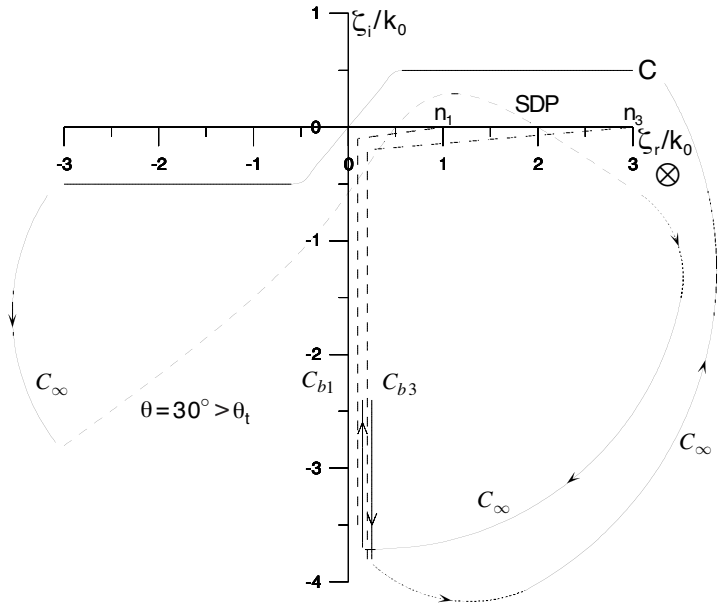

Figure 9. Proper closure of Re$\{\zeta\}$-axis inversion contour C into SDP and substrate branch cut for $\theta > \theta_t$: $n_1 = 1.,\ n_2 = 3.2,\ n_3 = 3.,\ \theta_t = 19.5°$.

path always violates the cover and substrate branch cuts C_{b1}, C_{b3} even number of times for $\theta < \theta_t$, where the threshold aspect angle is defined by

$$\theta_t = \sin^{-1}\left(\frac{n_1}{n_3}\right) = \frac{\pi}{2} - \cos^{-1}\left(\frac{n_1}{n_3}\right) \tag{40}$$

Hence both ends of the steepest-descent path lie on the top sheet and it does not need to be deformed about any of the branch cuts but can be directly connected to the Re$\{\zeta\}$-axis inversion contour on the top sheet of the 4-sheeted Riemann surface. It is noted that the specification of a radiation condition that is most conveniently stipulated as Re$\{p_1\zeta\} > 0$ implies that if the integration path stays on the top Riemann sheet in the complex ζ-plane. However, for $\theta \geq \theta_t$, the steepest-descent path violates the substrate branch cut an odd number of times and the left side of the steepest-descent path lies on the top sheet of the substrate layer Riemann surface while its right side ends on the bottom sheet. Therefore, the proper closure of the steepest-descent path to the Re$\{\zeta\}$-axis inversion contour forces the integration path to be deformed fully around the substrate branch cut so that both ends of the steepest-descent path lie on the top Riemann sheet as depicted in Fig. 9. Even if

the substrate wavenumber, $p_3(\zeta)$, stays on the bottom Riemann sheet during the integration path deformation, the contour from the one end of the steepest-descent path to the substrate branch cut, C_∞, the closure condition is still satisfied. This is because the exponents in the integrand of the field representation only contains the cover wavenumber, $p_1(\zeta)$, on the top sheet of 4-sheeted Riemann surface so that it can still converge.

$$\begin{aligned} &\oint_{C-SDP-C_{b3}-C_p-C_\infty} \Psi_1(x,z:\zeta)d\zeta = 0 \\ &\int_{C_p} \Psi_1(x,z:\zeta)d\zeta \to 0 \\ &\int_{C_\infty} \Psi_1(x,z:\zeta)d\zeta \to 0 \end{aligned} \tag{41}$$

where Ψ_1 represents the integrand of the cover field. Surface wave poles contributes negligibly to the radiation field and leaky wave poles captured on the lower sheet do not contribute to the radiation field. Hence the cover radiation field becomes in agreement with the radiation condition

$$\int_C \Psi_1(x,z:\zeta)d\zeta = \int_{SDP} \Psi_1(x,z:\zeta)d\zeta = \int_{C_{b3}} \Psi_1(x,z:\zeta)d\zeta \tag{42}$$

It is observed that the substrate branch cut contribution vanishes for $\theta < \theta_t$. Moreover the substrate branch cut contribution to the cover field is annulled in the far zone but in the near zone, the substrate branch cut contribution still remains. However, in the near zone, the corresponding wave arising from path deformation around the substrate branch cut is negligible near the threshold aspect angle, the field discontinuity due to the branch cut contribution is resolved so that the total radiation field is continuous over that region.

For TM case, the steepest-descent path on the complex ζ-plane is identically determined from Eqn. (39). Therefore, Fig. 8 also depicts the steepest-descent paths for the TM cover field in the complex ζ-plane for various observation aspect angles. As discussed earlier, for $\theta < \theta_t$, the steepest-descent path can be directly connected to the $\mathrm{Re}\{\zeta\}$-axis inversion contour on the top sheet of the 4-sheeted Riemann surface. However, it is observed that the integrands of the electric Green's dyads are contributed to by an electric charge distribution from the continuity equation within the source region [11] and [12]. Therefore,

$$\int_C \Psi^e_{lm\alpha\beta}(x,z|x',z':\zeta)d\zeta = \chi\delta(x-x')\delta(z-z')$$

$$+\int_{SDP}\Psi^e_{lm\alpha\beta}(x,z|x',z':\zeta)d\zeta \quad (43)$$
$$+\int_{C_p}\Psi^e_{lm\alpha\beta}(x,z|x',z':\zeta)d\zeta$$

where

$l=1,2,3 \quad m=1,2 \quad \text{and} \quad \alpha,\beta = x \text{ or } z$

where $\Psi^e_{lm\alpha\beta}$ denotes the integrand of the electric Green's dyad. Then,

$$\therefore \chi = \lim_{S'_\delta\to 0}\int_{S'_\delta}\left\{\int_C \Psi^e_{lm\alpha\beta}(x,z|x',z':\zeta)d\zeta - \int_{SDP}\Psi^e_{lm\alpha\beta}(x,z|x',z':\zeta)d\zeta\right.$$
$$\left. - \int_{C_p}\Psi^e_{lm\alpha\beta}(x,z|x',z':\zeta)d\zeta\right\}dx'dz' \quad (44)$$

where S'_δ is a small cross section of source region which contains the field point (x,z). Obviously, the magnetic Green's dyad is not affected by continuity equation. For $\theta \geq \theta_t$ as depicted in Fig. 9

$$\oint_{C-SDP-C_{b3}-C_p-C_\infty}\Psi^e_{lm\alpha\beta}(x,z|x',z':\zeta)d\zeta = 0$$
$$\oint_{C-SDP-C_{b3}-C_p-C_\infty}\Psi^h_{lm\alpha\beta}(x,z|x',z':\zeta)d\zeta = 0 \quad (45)$$

For the electric Green's dyad,

$$\int_C \Psi^e_{lm\alpha\beta}(x,z|x',z':\zeta)d\zeta = \chi\delta(x-x')\delta(z-z')$$
$$+\int_{SDP}\Psi^e_{lm\alpha\beta}(x,z|x',z':\zeta)d\zeta$$
$$+\int_{C_{b3}}\Psi^e_{lm\alpha\beta}(x,z|x',z':\zeta)d\zeta$$
$$+\int_{C_p}\Psi^e_{lm\alpha\beta}(x,z|x',z':\zeta)d\zeta \quad (46)$$

The pole and δ-function contributions vanish in the far zone. For the far zone magnetic Green's dyad,

$$\int_C \Psi^h_{lm\alpha\beta}(x,z|x',z':\zeta)d\zeta = \int_{SDP}\Psi^h_{lm\alpha\beta}(x,z|x',z':\zeta)d\zeta$$
$$+\int_{C_{b3}}\Psi^h_{lm\alpha\beta}(x,z|x',z':\zeta)d\zeta \quad (47)$$

Therefore, the integral path deformation is identical for both TE and TM cases.

7. STEEPEST-DESCENT EVALUATION OF SUBSTRATE FIELD

The steepest-descent path in the complex ζ-plane is obtained from Eqn. (27) in agreement with $l = 3$ for the substrate layer index. The saddle point of the steepest-descent path in the complex ζ-plane denoted by $k_3 \sin\theta$ exists near guided-mode pole singularities for certain aspect angles. Hence, the integrand of inverse spectral substrate field representation doesn't vary slowly near the saddle point, which forces the saddle point approximation to be failed at these angles in the substrate layer region. The steepest-descent paths in the complex ζ-plane on various observation aspect angles are depicted in Fig. 10. The integration path deformation for $\theta < \theta_t$ in the complex ζ-plane is identical to that for the cover field so it will not be repeated here. However, for $\theta \geq \theta_t$, the steepest-descent path violates cover branch cut an odd number of times and substrate branch cut an even number of times as depicted in Fig. 10 therefore it must be deformed about the cover branch cut partially to stay on the top Riemann sheet as depicted in Fig. 11. Then, after similar analysis for the cover field, the radiation field becomes

$$\int_C \Psi_3(x, z : \zeta) d\zeta = \int_{SDP} \Psi_3(x, z : \zeta) d\zeta + \int_{partial\{C_{b1}\}} \Psi_3(x, z : \zeta) d\zeta \tag{48}$$

where Ψ_3 represents the integrand of the substrate field. The partial path deformation was forced to satisfy the closure condition. The field discontinuity even due to the partial deformation of the integration contour about the cover branch cut is considerable near a threshold aspect angle but the complex field phase compensates for the discontinuity so that the total radiation field is still continuous over that region through that angle.

For TM case, the steepest-descent paths in the complex ζ-plane are identical to those for TE case. It was observed earlier that the steepest-descent path doesn't need to be deformed to one of the branch cuts but is connected to the $\mathrm{Re}\{\zeta\}$-axis inversion contour on the top Riemann sheet for $\theta < \theta_t$. For the magnetic Green's dyad,

$$\oint_{C-SDP-C_p-C_\infty} \Psi^h_{lm\alpha\beta}(x, z|x', z' : \zeta) d\zeta = 0 \tag{49}$$

which leads to

$$\int_C \Psi^h_{lm\alpha\beta}(x, z|x', z' : \zeta) d\zeta = \int_{SDP} \Psi^h_{lm\alpha\beta}(x, z|x', z' : \zeta) d\zeta \tag{50}$$

for the far zone.

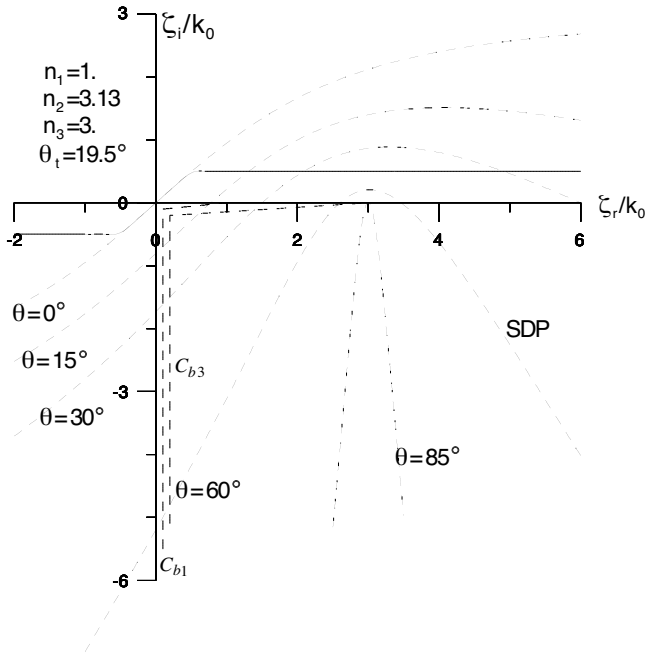

Figure 10. The steepest-descent paths for the substrate layer field calculation at various observation aspect angles in the complex axial spectral plane. The asymmetric planar dielectric waveguide consists of cover, guiding and substrate layers with indices $n_1 = 1,\ n_2 = 3.13$, and $n_3 = 3$ respectively.

It is previously observed that integrands of electric Green's dyads are contributed by the electric charge distribution implicated by the continuity equation within a source region. However, since $x \neq x'$ and $z \neq z'$ in the substrate layer the substrate electric Green's dyad is not relevant to the continuity equation. Therefore,

$$\int_C \Psi^e_{lm\alpha\beta}(x,z|x',z':\zeta)d\zeta = \int_{SDP} \Psi^e_{lm\alpha\beta}(x,z|x',z':\zeta)d\zeta$$
$$= \int_{C_b=C_{b1}+C_{b3}} \Psi^e_{lm\alpha\beta}(x,z|x',z':\zeta)d\zeta \quad (51)$$

Hence, it is noted that the steepest-descent contribution is equivalent to the branch cut radiation field contribution for $\theta < \theta_t$.

It is observed earlier that for $\theta \geq \theta_t$, only the partial integration path deformation around the cover branch cut can satisfy the closure

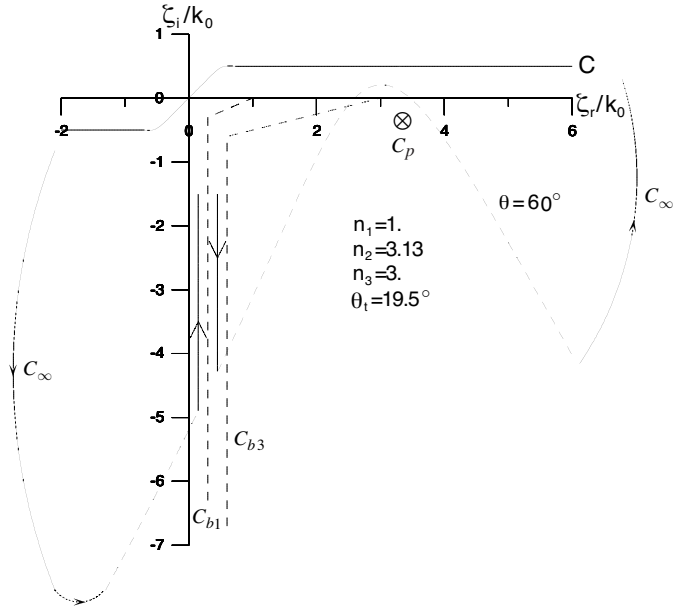

Figure 11. Proper closure of Re$\{\zeta\}$-axis inversion contour C into SDP and partial cover layer branch cut for $\theta > \theta_t$.

condition for the substrate field as depicted in Fig. 11.

$$\begin{aligned} \oint_{C-SDP-partial\{C_{b1}\}-C_p-C_\infty} \Psi^e_{lm\alpha\beta}(x,z|x',z':\zeta)d\zeta = 0 \\ \oint_{C-SDP-partial\{C_{b1}\}-C_p-C_\infty} \Psi^h_{lm\alpha\beta}(x,z|x',z':\zeta)d\zeta = 0 \end{aligned} \tag{52}$$

For the far-zone electric Green's dyad,

$$\begin{aligned} \int_C \Psi^e_{lm\alpha\beta}(x,z|x',z':\zeta)d\zeta &= \int_{SDP} \Psi^e_{lm\alpha\beta}(x,z|x',z':\zeta)d\zeta \\ &= \int_{partial\{C_{b1}\}} \Psi^e_{lm\alpha\beta}(x,z|x',z':\zeta)d\zeta \end{aligned} \tag{53}$$

And for the far-zone magnetic Green's dyad,

$$\begin{aligned} \int_C \Psi^h_{lm\alpha\beta}(x,z|x',z':\zeta)d\zeta &= \int_{SDP} \Psi^h_{lm\alpha\beta}(x,z|x',z':\zeta)d\zeta \\ &= \int_{partial\{C_{b1}\}} \Psi^h_{lm\alpha\beta}(x,z|x',z':\zeta)d\zeta \end{aligned} \tag{54}$$

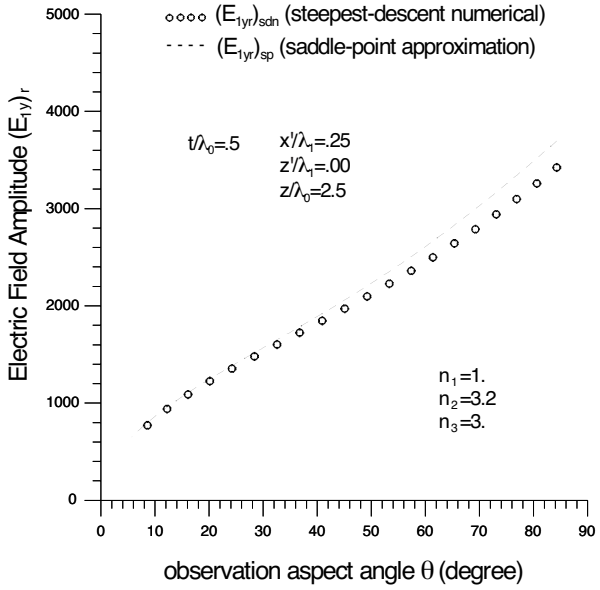

Figure 12. Transverse dependence of the reflected continuous spectrum in the cover layer; the steepest-descent numerical calculation and saddle-point approximation.

8. NUMERICAL RESULTS

The asymptotic radiation field of guiding structures is determined through the saddle-point approximation for far zone. But, in the near zone, the saddle-point method fails. The steepest-descent method in the complex ζ-plane is valid to determine the radiation field for both near and far zone. As depicted in Fig. 12, the small observation aspect angle θ corresponds to the far zone and the large one does to the near zone. Therefore, it is observed that the saddle-point approximation matches to the steepest-descent method in the far zone but, deviates from the steepest-descent method in the near zone.

During the steepest-descent contour in the cover layer, it is observed that both the partial and the full substrate layer branch cut deformations are acceptable for $\theta \geq \theta_t$ and the field discontinuity due to the full substrate branch cut contribution over θ_t can be resolved in the cover layer since the full branch cut contribution is negligible near the threshold aspect angle θ_t as depicted in Fig. 13.

In the substrate layer, the steepest-descent contour is equivalent to the remaining cover and full substrate branch-cut deformations as

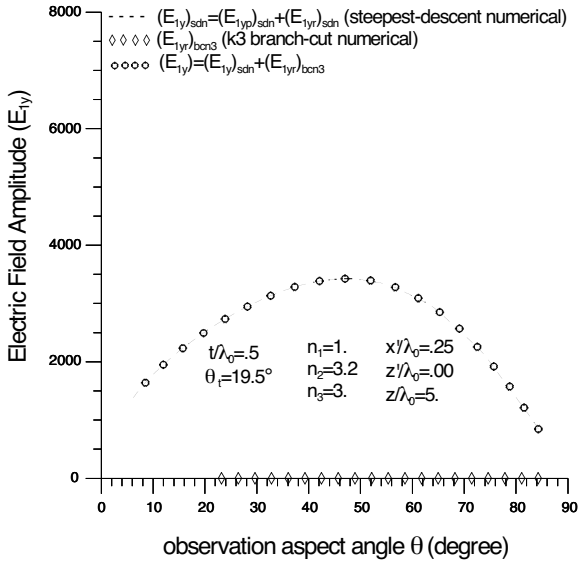

Figure 13. Transverse dependence of the continuous spectrum in the cover layer; steepest-descent numerical and the substrate layer branch cut.

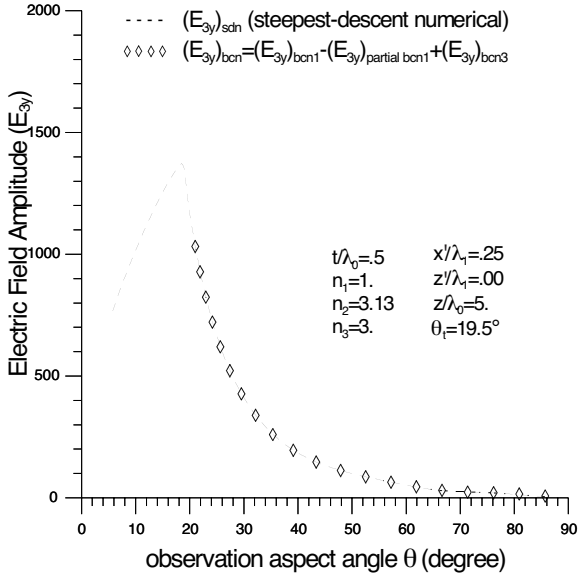

Figure 14. Transverse dependence of the transmitted spectrum in the substrate layer; steepest-descent numerical and the corresponding branch cuts.

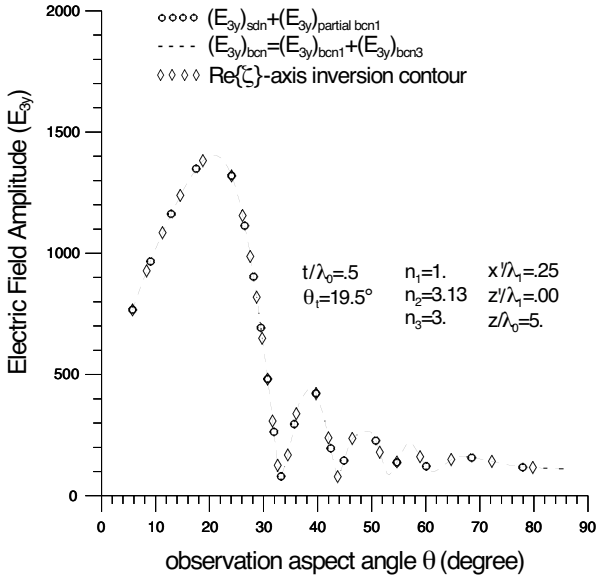

Figure 15. Transverse dependence of the transmitted spectrum in the substrate layer; steepest-descent numerical and the partial cover branch cut.

depicted in Fig. 14. Moreover, the partial cover branch cut contribution is considerable near θ_t but total field is still continuous over that angle since the field phase compensate the discrepancy and validated by Re$\{\zeta\}$-axis inversion contour integration as depicted in Fig. 15.

9. CONCLUSION

The steepest-descent path in the complex ζ-plane in both the cover and substrate layers was identified as a direct method and confirmed it using the transformation of the steepest-descent path in the complex ϕ-plane defined by $\phi = \sigma + j\eta$ as an indirect method. Both methods yielded the identical result and reconfirmed the validity. Using the steepest-descent method in the complex ζ-plane, the numerical evaluation of the TE radiation field can be implemented in both the cover and the substrate layer. During the steepest-descent implementation in the complex ζ-plane, the integral path must be deformed in order to meet the closure condition so that it can be properly connected to the Re$\{\zeta\}$-axis inversion contour. Then, the radiation field can satisfy Sommerfeld's radiation condition (closure

condition) and can be numerically validated by Re$\{\zeta\}$-axis inversion contour integration. Since the far-zone field is the main concern, the discrete-mode spectrum contributed by guided-pole singularity has been less emphasized.

Due to the intrinsic nature of TM mode excitation, Green's dyads for radiation fields can be formulated in both the cover and the substrate layers using the steepest-descent method in the complex ζ-plane. It is observed that the steepest-descent path in the complex ζ-plane is independent of the source excitatory mode but is dependent of the geometrical structure of the waveguide. Since the far-zone field is the main concern, the discrete mode spectrum contributed by guided-pole singularity was less emphasized like in TE mode. However, the discrete-mode spectrum for the electric Green's dyad must be considered significant within the near field and source regions. Charges contribute to the electric Green's dyad leading to a singularity term. Another important observation is that TM mode excitation cannot contribute to Green's dyad singularity for the magnetic field within the source region since no magnetic charge exists there.

During the steepest-descent contour deformation in both cover and substrate layers, it is observed that the corresponding branch cut deformation for each layer is identical for $\theta \geq \theta_t$ and the integration path deformation was reviewed earlier.

Since no numerical results for TM mode are presented in this paper, it is observed the apparent field discontinuity due to the branch cut contribution beyond the threshold aspect angle cannot be resolved numerically. However, based upon the results in TE case, it can be conjectured that either the branch cut contribution is negligible or the phase compensation for Green's dyad near the threshold aspect angle can resolve the field discontinuity in both cover and substrate layer regions. The rigorous numerical implementation for Green's dyad of the radiation field in both the near and far zones and also within the source region will be accommodated in future research.

APPENDIX A.

Spectral Green's dyads are given by

$$g^e_{11xx}(x|x') = \frac{1}{j\omega\varepsilon_1}\left\{\frac{\zeta^2}{2p_1}\left[e^{-p_1|x-x'|} + e^{-p_1(x+x')}\right] + \frac{2k_1^2}{p_1^2}\delta(x-x')\right\}$$

$$g^e_{11xz}(x|x') = -\frac{1}{j\omega\varepsilon_1}\frac{j\zeta}{2}\left[\mathrm{sgn}(x-x')e^{-p_1|x-x'|} - e^{-p_1(x+x')}\right]$$

$$g^e_{11zx}(x|x') = -\frac{1}{j\omega\varepsilon_1}\frac{j\zeta}{2}\left[\mathrm{sgn}(x-x')e^{-p_1|x-x'|} - e^{-p_1(x+x')}\right]$$

$$
\begin{aligned}
g^e_{11zz}(x|x') &= -\frac{1}{j\omega\varepsilon_1}\frac{p_1}{2}\left[e^{-p_1|x-x'|} - e^{-p_1(x+x')}\right] \\
g^e_{12xx}(x|x') &= -\frac{1}{j\omega\varepsilon_1}2\tilde{\Lambda}\varepsilon_1[\varepsilon_2 p_3\cosh(p_2 t) + \varepsilon_3 p_2\sinh(p_2 t)] \\
&\quad \cdot\frac{\zeta^2}{p_1^2}\left[\frac{e^{-p_1 x'}}{2} + \frac{\delta(x-x')}{p_1}\right]e^{-p_1 x} \\
g^e_{12xz}(x|x') &= \frac{1}{j\omega\varepsilon_1}j\zeta\tilde{\Lambda}\varepsilon_1[\varepsilon_2 p_3\cosh(p_2 t) + \varepsilon_3 p_2\sinh(p_2 t)]\frac{e^{-p_1(x+x')}}{p_1} \\
g^e_{12zx}(x|x') &= \frac{1}{j\omega\varepsilon_1}2\tilde{\Lambda}\varepsilon_1[\varepsilon_2 p_3\cosh(p_2 t) + \varepsilon_3 p_2\sinh(p_2 t)] \\
&\quad \cdot\frac{j\zeta}{p_1^2}\left[\frac{e^{-p_1 x'}}{2} + \frac{\delta(x-x')}{p_1}\right]e^{-p_1 x} \\
g^e_{12zz}(x|x') &= -\frac{1}{j\omega\varepsilon_1}\tilde{\Lambda}\varepsilon_1[\varepsilon_2 p_3\cosh(p_2 t) + \varepsilon_3 p_2\sinh(p_2 t)]e^{-p_1(x+x')} \\
g^e_{21xx}(x|x') &= \frac{1}{j\omega\varepsilon_1}2\tilde{\Lambda}\varepsilon_1\frac{\zeta^2}{p_1 p_2}\left[\frac{e^{-p_1 x'}}{2} + \frac{\delta(x-x')}{p_1}\right] \\
&\quad \cdot\{\varepsilon_2 p_3\sinh[p_2(x+t)] + \varepsilon_3 p_2\cosh[p_2(x+t)]\} \\
g^e_{21xz}(x|x') &= \frac{1}{j\omega\varepsilon_1}j\zeta\tilde{\Lambda}\varepsilon_1\{\varepsilon_2 p_3\sinh[p_2(x+t)] + \varepsilon_3 p_2\cosh[p_2(x+t)]\}\frac{e^{-p_1 x'}}{p_2} \\
g^e_{21zx}(x|x') &= \frac{1}{j\omega\varepsilon_1}2\tilde{\Lambda}\varepsilon_1\frac{\zeta^2}{p_1}\left[\frac{e^{-p_1 x'}}{2} + \frac{\delta(x-x')}{p_1}\right] \\
&\quad \cdot\{\varepsilon_2 p_3\cosh[p_2(x+t)] + \varepsilon_3 p_2\sinh[p_2(x+t)]\} \\
g^e_{21zz}(x|x') &= -\frac{1}{j\omega\varepsilon_1}\tilde{\Lambda}\varepsilon_1\{\varepsilon_2 p_3\cosh[p_2(x+t)] + \varepsilon_3 p_2\sinh[p_2(x+t)]\}e^{-p_1 x'} \\
g^e_{31xx}(x|x') &= \frac{1}{j\omega\varepsilon_1}2\tilde{\Lambda}\varepsilon_1\varepsilon_2\frac{\zeta^2}{p_1}\left[\frac{e^{-p_1 x'}}{2} + \frac{\delta(x-x')}{p_1}\right]e^{p_3(x+t)} \\
g^e_{31xz}(x|x') &= \frac{1}{j\omega\varepsilon_1}j\zeta\tilde{\Lambda}\varepsilon_1\varepsilon_2 e^{-p_1 x'}e^{p_3(x+t)} \\
g^e_{31zx}(x|x') &= \frac{1}{j\omega\varepsilon_1}2\tilde{\Lambda}\varepsilon_1\varepsilon_2 p_3\frac{j\zeta}{p_1}\left[\frac{e^{-p_1 x'}}{2} + \frac{\delta(x-x')}{p_1}\right]e^{p_3(x+t)} \\
g^e_{31zz}(x|x') &= -\frac{1}{j\omega\varepsilon_1}\tilde{\Lambda}\varepsilon_1\varepsilon_2 p_3 e^{-p_1 x'}e^{p_3(x+t)} \\
g^h_{11yx}(x|x') &= \frac{j\zeta}{p_1}\left[\frac{e^{-p_1|x-x'|}}{2} + \frac{e^{-p_1(x+x')}}{2} + \frac{2\delta(x-x')}{p_1}\right]
\end{aligned}
$$

$$g^h_{11yz}(x|x') = \frac{1}{2}\left[\mathrm{sgn}(x-x')e^{-p_1|x-x'|} - e^{-p_1(x+x')}\right]$$

$$g^h_{12yx}(x|x') = -2\tilde{\Lambda}\varepsilon_1[\varepsilon_2 p_3\cosh(p_2 t) + \varepsilon_3 p_2\sinh(p_2 t)] \cdot\frac{\zeta}{p_1^2}\left[j\frac{e^{-p_1 x'}}{2} + \frac{\delta(x-x')}{p_1}\right]e^{-p_1 x}$$

$$g^h_{12yz}(x|x') = \tilde{\Lambda}\varepsilon_1[\varepsilon_2 p_3\cosh(p_2 t) + \varepsilon_3 p_2\sinh(p_2 t)]\frac{e^{-p_1(x+x')}}{p_1}$$

$$g^h_{21yx}(x|x') = 2\tilde{\Lambda}\varepsilon_2\frac{j\zeta}{p_1 p_2}\left[\frac{e^{-p_1 x'}}{2} + \frac{\delta(x-x')}{p_1}\right] \cdot\{\varepsilon_2 p_3\sinh[p_2(x+t)] + \varepsilon_3 p_2\cosh[p_2(x+t)]\}$$

$$g^h_{21yz}(x|x') = -\tilde{\Lambda}\varepsilon_2\{\varepsilon_2 p_3\sinh[p_2(x+t)] + \varepsilon_3 p_2\cosh[p_2(x+t)]\}\frac{e^{-p_1 x'}}{p_2}$$

$$g^h_{31yx}(x|x') = 2\tilde{\Lambda}\varepsilon_2\varepsilon_3\frac{j\zeta}{p_1}\left[\frac{e^{-p_1 x'}}{2} + \frac{\delta(x-x')}{p_1}\right]e^{p_3(x+t)}$$

$$g^h_{31yz}(x|x') = -\tilde{\Lambda}\varepsilon_2\varepsilon_3 e^{-p_1 x'}e^{p_3(x+t)}$$

REFERENCES

1. Stratton, J. A., *Electromagnetic Theory*, McGraw-Hill, New York, 1941.
2. Tai, C. T., "Effect of a grounded slab on radiation from a line source," *J. Appl. Phys.*, Vol. 22, 1951.
3. Tamir, T. and A. A. Oliner, "Guided complex waves. I. Fields at an interface. II. Relation to radiation patterns," *Proc. IEE (London)*, Vol. 110, 1963.
4. Felsen, L. B. and N. Marcuvitz, *Radiation and Scattering of Waves*, Chapter 5, Prentice-Hall, Englewood Cliffs, N.J., 1973.
5. Nyquist, D. P., "Leaky-wave and radiation modes of the planar dielectric waveguide — A review of their origin and significance," *International Symposium on Electromagnetic Theory*, Thessaloniki, Greece, 1998.
6. Nyquist, D. P., "Asymptotic radiation field of asymmetric planar dielectric waveguide," *Mathematical Methods in Electromagnetic Theory*, Kharkov, Ukraine, 1998.
7. Tai, C. T., "On the eigenfunction expansion of dyadic Green's functions," *Proc. IEEE*, Vol. 61, 1973.
8. Viola, M. S. and D. P. Nyquist, "An observation on the

Sommerfeld-integral representation of the electric dyadic Green's function for layered media," *IEEE Trans. Microwave Theory and Techniques*, Vol. MTT-36, 1289–1292, 1988.

9. Chew, W. C., "Some observations on the spatial and eigenfunction representations of dyadic Green's functions," *IEEE Trans. Microwave Theory and Techniques*, Vol. MTT-37, 1322–1327, 1989.
10. Chew, W. C., *Waves and Fields in Inhomogeneous Media*, Van Nostrand Reinhold, New York, 1990.
11. Rahmat-Samii, Y., "On the question of computation of dyadic Green's function at the source region in waveguides and cavities," *IEEE Trans. Microwave Theory and Technique*, Vol. MTT-23, 1975.
12. Yaghjian, A. D., "Electric dyadic Green's functions in the source region," *Proc. IEEE*, Vol. 68, 1980.